Machine learning and individual variability in electric field characteristics predict tDCS treatment response

Alejandro Albizu[a,b], **Ruogu Fang**[a,c], **Aprinda Indahlastari**[a,d], **Andrew O'Shea**[a,d], **Skylar E. Stolte**[c], **Kyle B. See**[c], **Emanuel M. Boutzoukas**[a,d], **Jessica N. Kraft**[a,b], **Nicole R. Nissim**[a,b], **Adam J. Woods**[a,b,d,*]

[a]Center for Cognitive Aging and Memory, McKnight Brain Institute, University of Florida, Gainesville, USA

[b]Department of Neuroscience, College of Medicine, University of Florida, Gainesville, USA

[c]J. Crayton Pruitt Family Department of Biomedical Engineering, Herbert Wertheim College of Engineering, University of Florida, Gainesville, USA

[d]Department of Clinical and Health Psychology, College of Public Health and Health Professions, University of Florida, Gainesville, USA

Abstract

Background: Transcranial direct current stimulation (tDCS) is widely investigated as a therapeutic tool to enhance cognitive function in older adults with and without neurodegenerative disease. Prior research demonstrates that electric current delivery to the brain can vary significantly across individuals. Quantification of this variability could enable person-specific optimization of tDCS outcomes. This pilot study used machine learning and MRI-derived electric field models to predict working memory improvements as a proof of concept for precision cognitive intervention.

Methods: Fourteen healthy older adults received 20 minutes of 2 mA tDCS stimulation (F3/F4) during a two-week cognitive training intervention. Participants performed an N-back working memory task pre-/post-intervention. MRI-derived current models were passed through a linear Support Vector Machine (SVM) learning algorithm to characterize crucial tDCS current

components (intensity and direction) that induced working memory improvements in tDCS responders versus non-responders.

Main results: SVM models of tDCS current components had 86% overall accuracy in classifying treatment responders vs. non-responders, with current intensity producing the best overall model differentiating changes in working memory performance. Median current intensity and direction in brain regions near the electrodes were positively related to intervention responses ($r = 0.811$, $p < 0.001$ and $r = 0.774$, $p = 0.001$).

Conclusions: This study provides the first evidence that pattern recognition analyses of MRI-derived tDCS current models can provide individual prognostic classification of tDCS treatment response with 86% accuracy. Individual differences in current intensity and direction play important roles in determining treatment response to tDCS. These findings provide important insights into mechanisms of tDCS response as well as proof of concept for future precision dosing models of tDCS intervention.

Keywords

Transcranial direct current stimulation; tDCS; Cognitive aging; Finite element modelling; Machine learning; Treatment response

1. Introduction

For almost two decades, transcranial direct current stimulation (tDCS) has been instrumental in advancing the knowledge of human brain function by altering neural activity in the brain [1–3]. tDCS has been suggested to alter resting membrane potentials (*i.e.*, modulate or attenuate), influencing neuronal excitability across the local field of stimulation [1–5]. With this, tDCS has shown great promise as a therapeutic intervention in various neurological and psychiatric disorders [6–9]. While the number of tDCS applications within the literature has grown exponentially [1–5], the optimal dosing parameters (*e.g.*, applied current, electrode placement, *etc.*) that underlie the positive effect of tDCS remain unclear.

Prior research shows that increasing or decreasing the intensity of applied stimulation to the scalp results in corresponding changes in the electric field within the brain [10]. *In vitro* studies have shown that the intensity component of tDCS current can modulate cortical excitability [11,12]. Experimental and theoretical studies have indicated that tDCS-related electric field intensity is essential for altering neuron resting membrane potentials and modification of synaptic strength (*i.e.*, LTP/LTD) [13–17]. Studies show that increased applied current intensity is associated with increased amplitude of motor evoked potentials (MEPs), suggesting neuronal sensitization of the motor cortex [8,18–20]. Therefore, varying levels of applied current intensity in tDCS may lead to changes in behavioral outcomes.

Furthermore, electrode placements during tDCS can greatly affect the distribution and direction of electric current throughout the brain [21,22]. Whole-cell recordings have demonstrated that electric field orientation is essential to the likelihood of neuronal firing [23]. Neuronal bodies in parallel with the direction of applied electric fields are more susceptible to stimulation responses. Human studies have also highlighted the importance of tDCS current direction for modulating cortical excitability [24,25]. Rawji *et al.* (2018)

evaluated individual effects of tDCS montages that produced electric fields oriented orthogonal or parallel to the motor cortex on the modulation of MEPs. The orthogonal montage was observed to have greater current flow normal to the cortical surface (*i.e.*, current flow in parallel with the dendritic axis of cortical neurons). These authors reported significant alterations in MEPs with this montage compared to sham [25]. These data suggest that the direction of current flow in the tDCS electric field may be strongly correlated with behavioral outcomes of tDCS.

Conventional tDCS typically employs a fixed applied current (*e.g.*, 2 mA) and electrode placement (*e.g.*, F3/F4) across participants [26]. However, the orientation and intensity of the generated electric field within cortical tissue can be dramatically altered by inter-individual anatomical differences. For instance, brain atrophy can reduce the level of current reaching the brain due to an increase in current shunting within cerebrospinal fluid (CSF) [27,28]. Individual skull thickness and subcutaneous adipose tissue volume can also alter voltage delivery due to differences in tissue conductivity [29–32].

MRI-derived finite element models (FEM) can be used to estimate individualized electric field induced by tDCS. Advancements in tissue segmentation tools and automated modeling pipelines [33,34] have enabled more efficient generation of large and complex FEM that would normally require extensive computing power and time. These models have recently been compared to experimental results obtained via a novel *in-vivo* magnetic resonance electrical impedance tomography technique [35,36] and intracranial recordings [22,37]. While the experimental results showed a strong correlation with computational model outcomes, a large variation across individuals was observed. Therefore, investigating the nuance of electrical distribution in individualized models may provide more insight into inter-individual variability seen with tDCS. However, the size (*i.e.*, millions of voxels across multiple dimensions) and complexity of generated electric fields has made interpretation of the essential current characteristics (*i.e.*, current direction, intensity, *etc.*) challenging.

Few studies have attempted to systematically investigate these estimates of electric field distributions as a predictor of responses to tDCS [38–40]. All three prior studies reported increases in current intensity associated with increases in the target behavioral response (*e.g.*, self-reported and physiological measures) [38–40]. Antonenko *et al.* also reported a positive relationship between the current direction normal to the cortical surface and sensorimotor network strength [40]. These studies employed univariate approaches that treat each voxel or region of interest within the brain as an independent predictor of treatment response. At present, no studies have employed multivariate approaches to investigate patterns within the current distribution as a predictor of treatment response.

Supervised machine learning methods (*e.g.*, support vector machines; SVM) constitute a novel approach in neuroimaging to investigate large and complex datasets [41–44]. SVM uses Mercer's Theorem [45], which allows the representation of high dimensional feature space in a low-dimensional Gram matrix (Equation (4)) – also known as the "kernel trick" [46]. SVM performs multivariate analyses across many voxels to classify patterns of information [41] that can be used to identify individual contributions of current intensity and direction towards behavioral responses. Multivariate classifiers are iteratively trained to

search for patterns within the data that best predict a specified prognostic label, such as behavioral response. This is usually achieved within a cross-validation procedure, withholding a different partition of data for each iteration of training. This is a standard approach within the statistical literature and a widely used technique to provide unbiased generalizability to new data samples [42–44,47]. One study used machine-learning of clinical data to predict treatment responses [48]; however, there are currently no studies that utilize machine learning on FEM to investigate the critical components of dosing parameters in tDCS.

Previous work from our research group demonstrated working memory improvements in older adults following tDCS paired with cognitive training [49]. The objective of this study was to apply machine learning and FEM in the same dataset and identify the central determinants of treatment response. Specifically, the present study applied an SVM machine-learning algorithm to investigate the contributions of current intensity and direction, as well as their interaction, for predicting working memory improvements in older adults. Our primary hypothesis is that SVM applied to individualized tDCS current models are capable of classifying tDCS responders and non-responders above chance (*i.e.*, area under the curve > 0.5). In addition, we hypothesized that the interaction of direction and intensity is the most essential dosing feature for predicting behavioral response. These data will provide critical insight to inform tDCS mechanism theory and provide a potential foundation for methods to increase the effectiveness of tDCS applications.

2.   Methods

Structural imaging and behavioral data were sourced from a phase-II pilot clinical trial that employed a randomized, triple-blinded (assessor, interventionist, participant) design (NCT02137122). This approach enabled examination of the combined effects of tDCS with cognitive training on working memory function in healthy older adults [49].

2.1.   Participants

Fourteen healthy older adults receiving active-tDCS stimulation were selected for further analysis by the current study [mean (sd) age = 73.57 (7.84), mean MoCA = 27.85 (1.79), 7F:7M]. All participants were screened for eligibility based on study inclusion criteria detailed in the prior manuscript [47]. The study protocol was in accordance with the Declaration of Helsinki and approved by the University of Florida's Institutional Review Board. Informed written consent was obtained from participants prior to study procedures.

2.2.   tDCS protocol and application

Conventional 1×1 tDCS (Soterix Medical, tDCS-CT for clinical trials) was applied using two $5 \times 7cm^2$ pad electrodes presoaked with 2 mL of 0.9% NaCl and 4 mL added per side (10 mL total per sponge) at F3 (cathode) and F4 (anode) location. Participants underwent head measurements using the International 10–20 system to locate F3–F4 locations at each session. Participants were stimulated at 2 mA intensity for 20 minutes with a 30-second current ramp up and down, with a total of 10 stimulation sessions over 14 days. Each session included 40-minute computerized cognitive training for working memory with stimulation

delivered during the first 20 minutes. Details of the computerized training tasks are described in the previous publication [49]. No significant effects of unblinding or differences in sensation were found for active vs. sham participants in the parent study [49].

2.3. Behavioral tasks

Participants' working memory was assessed with an in-scanner N-back task only given at baseline and post-intervention. The task paradigm for each run consisted of four blocks of two-back and four blocks of zero-back presented in a randomized order with 20 seconds of rest between blocks. During the two-back, participants viewed uppercase letters, one at a time. A screen with a central crosshair (+) was presented during the inter-trial interval (Fig. 1). The stimuli appeared for 1 second, followed by a crosshair for 3 seconds, providing a 4-second window to make a response. Details of the N-back task procedure are outlined in the prior paper [49]. Participants performed practice on the N-back task (two- and zero-back) outside of the scanner to ensure understanding of the task at both baseline and post-intervention visits. Two-back performance change (*i.e.*, pre-/post-intervention) was analyzed as a composite percent improvement score for accuracy and reaction time $\left(\frac{\Delta ACC + \Delta RT}{2}\right)$.

2.4. Imaging sequences and parameters

Structural T1-weighted MRI scans were obtained using a 32-channel, receive-only head coil from a 3-T Siemens MAGNETOM Prisma MRI scanner. MPRAGE sequence parameters included: repetition time (TR) = 1800 ms; echo time (TE) = 2.26 ms; flip angle = 8°; field of view (FOV) = $256 \times 256 \times 176$ mm; voxel size = 1 mm^3.

2.5. Computational model construction

Individual T1-weighted images were converted from DICOM to NIfTI using dcm2niix [50] and resampled with the FreeSurfer v6.0.0 image analysis suite (http://surfer.nmr.mgh.harvard.edu/) into a 256 mm^3 field of view (RAS orientation), 1 mm^3 voxel size. The computational models of current density were computed using the Realistic vOlumetric-Approach to Simulate Transcranial Electric Stimulation (ROAST; https://www.parralab.org/roast/) toolbox [33] with parallel processing on a high performance cluster with 50 CPU cores and 175 GB of RAM provided by the Research Computing at the University of Florida (HiPerGator). The resampled T1 images ($256 \times 256 \times 256$, 1 mm^3) were individually processed in parallel using ROAST. The segmentation process was carried out in FreeSurfer to classify tissue types into gray and white matter. FreeSurfer segmentations were visually inspected and manually corrected for errors before reprocessing through FreeSurfer – a procedure that has been validated against manual segmentation [51] and histological measures [52]. Segmentations from FreeSurfer were then combined with segmented CSF, bone, skin, and air from ROAST (See Supplemental Fig. 1). Combined segmented tissues were visually inspected for unassigned voxels to ensure every voxel within the head volume was assigned to one of the six tissue types by overlaying individual segmented volumes with their respective T1 images. Default isotropic conductivity values (gray matter: 0.276 S/m; white matter: 0.126 S/m; CSF: 1.65 S/m; bone: 0.01 S/m; and skin: 0.465 S/m) were assigned to each tissue in ROAST [33]. Volumetric meshes of each tissue type were generated using iso2mesh [53]. Boundary conditions were assigned within

ROAST and a finite element solver, getDP [54], was used to compute voltage solutions to the Laplace equation, in the meshed models, where V is the electric potential within the volume and σ is the tissue conductivity. Additional MATLAB routines to compute current density (J) from electric field (E) and tissue conductivity (σ) were added in accordance with Ohm's law: $J = \sigma E$. Current density (J) is a useful metric for determining the dosage of current (A/m^2) induced in the brain from electrical stimulation. Current density also represents a unit of current directly adjustable through alteration of applied stimulation intensity (*e.g.*, 2 mA vs. 2.3 mA) for the purposes of individualized dosing calculations.

The intensity of current at each voxel was calculated with the function:

$$\vec{J} = \sqrt{J_x^2 + J_y^2 + J_x^2} \tag{1}$$

Direction of current density in each coordinate plane was separated from intensity by deriving the zenith angle, θ, between $\vec{J}$ and the *z*-axis, and the azimuthal angle, φ, between the projection of $\vec{J}$ onto the *xy*-plane, $\vec{J}'$ and the *x*-axis:

$$\theta = \cos^{-1} \frac{J_z}{\sqrt{J_x^2 + J_y^2 + J_z^2}} \tag{2}$$

$$\varphi = \tan^{-1} \frac{J_y}{J_x} \tag{3}$$

2.6. Electrode placements

Conventional electrodes (5×7 cm^2) were constructed from 3D captured electrode models as reported in our previous publication [26] and added to the segmented models in ROAST. Individual electrode placement variability per session for each participant can be found in Supplemental Fig. 3. Default conductivity values of 5.9×10^7 S/m and 0.3 S/m were assigned to the electrode and gel layers, respectively [55]. A +2 mA voltage boundary condition was assigned to the anode electrode at the F4 location, while a −2 mA voltage boundary condition was assigned to the cathode electrode at the F3 location (Fig. 2). Precise electrode locations were recorded for each session with a 3D scanner mounted to an iPad. 3D images were converted to a surface mesh via TechMed3D's MSoft software [TechMed 3D, Quebec City]. More details of this procedure can be found in a previous publication [26]. Electrode information from each session was added to individual segmented tissue volumes prior to creating volume meshes and solving finite element models, totaling 10 unique head models per individual. Individual, as well as grouped, average and variance maps of current density per electrode placement can be found in Supplemental Figs. 5–8. Electrode displacement was computed as the 3D Euclidean distance between modeled electrodes and the ideal location of F3–F4 derived from ROAST [55].

2.7. Supervised machine-learning

Current density values were computed in native space then masked using individual participants' white and gray matter voxels to restrict current values within brain region only and reduce the number of features submitted into the classifier. Masked values were then transformed with the University of Florida Aging Brain-587 tissue probability map [28] into MNI space using SPM's normalise function [56]. Median values of $\overrightarrow{J}$ before and after the transformation were computed as a quality check for transformation errors ($r = 0:998$). Participant classes were determined by separating participants into binary groups based on pre-/post-intervention performance changes on the two-back working memory task above or below the median. The tDCS responder class ($n = 7$) had an average performance increase of 22%, whereas, the tDCS non-responder class ($n = 7$) was found to have an average 9% increase in two-back performance ($F(1) = 21:02$, $p < 0.001$). No significant differences in age ($p = 0:89$), sex ($p = 0:66$), education ($p = 0:53$), cortical atrophy ($p = 0:22$), nor any normalized tissue volume (See Supplemental Figs. 1–2) between these groups were observed.

Due to the high dimensionality of MRI data, feature selection was performed on the training data to further reduce the number of trained features. One popular method of feature selection is to filter the features via voxel wise t-tests between classes to select current elements with a significant group-level difference ($p < 0:01$) as features for the subsequent prediction step [42,57,58]. To classify responders from non-responders, we used Support Vector Machine (SVM), a machine learning algorithm to search for the optimal hyperplane that separates two classes with maximal margin under the assumption of independently and identically distributed (iid) data [59], which is satisfied in this study. Specifically, LIBSVM [41] was used to optimize the objective function:

$$\min_{w,b} \frac{1}{2} w^T w + C \sum_{i=1}^{l} \max\left(1 - y_i\left(w^T x_i + b\right), 0\right)^2 \tag{4}$$

where $C \quad 0$ is a penalty parameter on the training error. A linear kernel K was generated with the function:

$$K\left(x_i, x_j\right) = x_i^T x_j \tag{5}$$

Model performance was evaluated across ten permutations of two-level nested stratified cross-validation [60–62]. To elaborate, we began by splitting the data into K-folds (in this case K = 7) and performed an outer cross-validation loop consisting of K iterations. In each iteration, K-1 folds were used as training data with a single fold left out as test data. A second, inner cross-validation loop was then performed on the training data, providing us with optimal hyper-parameter C. Following training, predictions of held out test data, x, were performed with the decision function:

$$f(x) = sgn\left(w^T x + b\right) \tag{6}$$

After all K iterations in the outer cross-validation loop were performed, predicted labels of all subjects were compared against ground truth labels to calculate performance metrics. A receiver operating characteristic (ROC) curve of true positive rate against false positive rate was plotted to demonstrate the separability of classes within each model by calculating the area under the ROC curve (AUC). To assess the stability of feature weights, the standard deviation of feature weights across folds were plotted (see Supplemental Fig. 9). For feature weight generation and deployment, a final model was trained on all fourteen current density maps to derive overall classification weights, w (*i.e.*, the model parameters learned by the optimization function during the training phase, *cf.* Equation (3)). These weights can be applied to independent data from a new subject to predict their tDCS response classification associated with specific observed *J*-map features in test data. The feature weights at each voxel, representing the relative contribution of each voxel to the classification, were separated by positive and negative weights that predict responders and non-responders, respectively [63]. Positive and negative weights were divided by their respective sum of weights to compute the percent contribution of each voxel toward either positive or negative predictions. To demonstrate specific brain regions that predict working memory improvements, regions of interest (ROIs) were defined using the Harvard-Oxford atlas [64] and ranked based on their average voxel percent contribution.

2.8. Statistical analyses

SPSS Statistics 25 (https://www.ibm.com/analytics/spss-statistics-software) and the Statistics and Machine Learning toolbox in MATLAB 2019b [65] were used to carry out statistical analyses. One-way ANOVA was used to assess mean difference in model performance between the three data types (direction, intensity, direction x intensity). A secondary set of analyses was aimed at determining the characteristics of current within the voxels determined to be essential for treatment response. Within these regions, Pearson's correlation analyses were used to assess the relationship of behavioral response with field characteristics. Linear regression analyses were used to fit lines of least square residuals. Hedge's *g* was computed to define effect sizes of mean differences, corrected for small sample bias [66]. Since all fourteen participants in our study were individuals with no familial relationship and each participant's data were collected under the same condition, these data points met the statistical assumptions of independently and identically distributed (iid) data. To determine the normality of each variable, we tested the null hypothesis that each data vector comes from a standard normal distribution, against the alternative that it does not come from such a distribution, using the one-sample Kolmogorov-Smirnov test [67,68]. The null hypothesis of a normal distribution was not rejected by the Kolmogorov-Smirnov test for all variables analyzed.

To quantify the required input current for converting non-responders into the responder range, the formula:

$$\hat{I} = I_o\left(1 + \frac{\bar{J} - x}{x}\right) \tag{7}$$

where x represents a non-responder mean current value, $\bar{J}$ represents the target current values (*i.e.*, average values computed in the responder group), I_o represents the original

injected current (*e.g.*, 2 mA), and $\frac{\bar{J} - x}{x}$ represents the percent difference. The optimal electrode displacement was defined as the mean responder displacement minus the non-responder displacement.

3. Results

3.1. Machine learning predictions of tDCS intervention efficacy

Computational models of current intensity, current direction, and their interaction, all demonstrated above chance performance for classifying treatment responders (*i.e.*, AUC>50%). The AUC revealed that the probability of current intensity model to rank a randomly chosen responder higher than a randomly chosen non-responder was 80.6% (Fig. 3A) [69]. Classification of the direction alone and combined models of direction and intensity produced AUCs of 77.6% and 74.9%, respectively. A summary of model performances can be found in Table 1. Computational models of current intensity alone marginally outperformed current direction and the combination of current direction with intensity in the classification problem (Fig. 3B). However, a one-way ANOVA between the AUC of each current characteristic ($F(2) = 1.31$, $p = 0.288$) revealed a non-significant difference between the three variables. The support vector machine classification of all three models correctly differentiated tDCS responders from non-responders with averaged overall accuracy of 86.43%. The 95% confidence interval of classification accuracy for these models was between [CI: 85.03–87.83%].

3.2. Field characteristics within voxels predictive of treatment responders

Within the voxels that discriminate tDCS responders from non-responders (Fig. 4), responders were found to have greater current intensity within these regions (Fig. 5A–B), with greater median ($r = 0.811$, $p < 0.001$) and mean current intensity ($r = 0.720$, $p = 0.004$) correlated with treatment response (Fig. 5C). Responders produced an effect size of 5.63 (Hedges' g; Fig. 5D) with a 95% confidence interval between [CI: 3.82–7.94] and a significant two-sided permutation *t*-test ($p < 0.001$, 5000 permutations). Behavior change was also related to the azimuthal angle, the angle of the current vector in the axial plane between the electrodes, φ ($r = 0.774$, $p = 0.001$) and the *x*-magnitude of the current vector, J_x ($r = 0.832$, p < 0.001). Behavior change was not related to zenith angle, θ ($r = 0.289$, $p = 0.32$; see Supplemental Fig. 4), *y*-magnitude of the current vector, J_y ($r = 0.222$, $p = 0.45$), or the *z*-magnitude of the current vector, J_z ($r = 0.281$, $p = 0.33$). Thus, current angled toward the cathode related to positive outcomes (see Fig. 6A–C for representative model). On average, the current direction computed within the *xy*-plane, φ, showed greater percentages of positive angles in responders, whereas non-responders demonstrated greater percentages of negative angles. Thus, an enhanced convergence of current direction toward the cathode was found within responders (Fig. 6D). Shifts in electrode location were also inversely correlated with behavior change (anode: $r = -0.732$, $p = 0.003$, cathode: $r = -0.775$, $p = 0.001$), as well as changes in median current intensity (anode: $r = -0.523$, $p = 0.06$, cathode: $r = -0.632$, $p = 0.02$) and azimuthal angle (anode: $r = -0.579$, $p = 0.03$, cathode: $r = -0.794$, $p < 0.001$) within these voxels.

3.3. Evaluation of simplified SVM models.

To determine whether the complexity of the original model presented in the current paper is required to achieve sufficient model performance, we assessed a set of simplified SVM models. As electrode displacement was strongly associated with behavior change, we trained an SVM to classify responder and non-responders based on only electrode displacement. In addition, prior research argues that tDCS primarily impacts only gray matter regions. As such, we trained an SVM to classify reponders and non-responders using only current characteristics from gray matter regions. These models did not outperform the original model (see Supplemental Table 1 and Supplemental Table 2; respectively).

3.4. Regional contributions toward predictions of tDCS response

Fig. 7A–B illustrates the top ten ranked ROIs based on the mean percent contribution per voxel within each region. See Fig. 7C for the distribution of percent contribution across Harvard-Oxford ROIs. The top ten ROIs that predicted working memory improvements were largely located in the frontal region underneath and between the electrodes (Fig. 7A). These ROIs were labelled as the: 1) Right Superior Frontal Gyrus, 2) Left Superior Frontal Gyrus, 3) Right Middle Frontal Gyrus, 4) Left Putamen, 5) Right Frontal Pole, 6) Right Precentral Gyrus, 7) Left Frontal Pole, 8) Right Pars Opercularis, 9) Left Caudate, 10) Right Supramarginal Gyrus, anterior division (Fig. 7B).

3.5. Dosing charactersitics in responders and non-responders

Equation (6) was used to determine the optimal dosing parameters that are likely to convert non-responders into responders. To match the mean profile of current characteristics demonstrated in responders, non-responders would require an average increase of applied current intensity to 4.3 mA [range(sd): 3.19–5.37 (0.71) mA] and shift in the cathode location 1.25 cm [range(sd): 0.52–2.22 (0.59) cm] closer to its ideal 10–20 location (F3). Fig. 8A and B demonstrate the relationship between differences in electrode placement and behavioral response. Fig. 8C and D demonstrate the required shifts in intensity (8C) and electrode placement (8D) to match the mean profile of responders.

4. Discussion

The present study investigated the essential characteristics of tDCS current (*i.e.*, current intensity, current direction, *etc.*) by using a machine learning algorithm to predict tDCS effects on measured behavioral outcomes. Overall, both current direction and intensity are demonstrated to be critical components of stimulation response. Consistent with our primary hypothesis, the electric field components produced predictions of tDCS response classification beyond chance (*i.e.*, AUC > 50%). While current intensity did marginally outperform other variables, this difference was not statistically significant. Contrary to our second hypothesis, all tested variables were comparable in classifying responders and non-responders. Considering each of these datatypes are derived from the same data vector, it is likely that the interaction of direction and intensity does not provide sufficient new information to outperform intensity alone. Since the SVM relies on pattern similarities between observations to make predictions, the interaction term of direction and intensity did not explain a significant level of new variance that was not already explained by the separate

main effects of intensity and direction. Using a small clinical trial dataset, the machine-learning algorithm presented in this paper provides proof of concept that an SVM was able to classify tDCS responders and non-responders with 86% accuracy based on patterns of current characteristics.

4.1. Characteristics of current

The weights produced by the SVM algorithm revealed the brain regions that contributed most to predictions of treatment response category. Within these regions, median and mean current intensity were found to positively relate to behavioral response, suggesting greater current intensity may produce greater behavioral response. Since tDCS is typically applied at a fixed dose across individuals, individual differences in anatomy are likely to cause varying amounts of current intensity within these essential brain regions. For instance, those with greater degrees of brain atrophy would have a decreased level of current intensity within stimulated brain tissues and thus may experience reduced efficacy from fixed dose tDCS. It is important to note that while our data demonstrate an association between delivering larger amounts of current intensity and better behavioral responses, this does not necessarily mean that "more is better" universally. For instance, Samani *et al.* previously reported that applied current doses beyond 2 mA demonstrates nonlinear alterations in neuronal excitability [70]. Thus, within the range of current intensities inducible in the brains of older adults receiving fixed 2 mA dose, increased current intensity appears beneficial for treatment response. Applied current doses beyond this range require further research. Electrode orientation and location during tDCS can also dictate the shape and location of stimulation contact area, altering the pattern of current flow within the brain [22]. Both anode and cathode displacement were found to negatively affect intensity and direction of current within the brain as well as behavioral response. Minor electrode shifts (*i.e.*, 1 cm) have been previously demonstrated to dramatically alter the current intensity by up to 38% [21,71]. Therefore, monitoring and increasing electrode placement accuracy via 3D capture techniques [26] may improve individual treatment response.

4.2. Regions of importance

The top ten ROIs that predict working memory improvements included the dorsolateral prefrontal cortex (DLPFC), ventrolateral prefrontal cortex (VLPFC), basal ganglia, and cingulo-opercular network regions [72]. The DLPFC and VLPFC are critically involved in monitoring, maintaining, and manipulating task-relevant information. These processes are vital for working memory function [73–75]. Recent studies have reported increased functional connectivity within these regions paired with improvements in working memory performance following applications of tDCS [49,76].

The basal ganglia also play an important role in learning and memory [77]. Specifically, the basal ganglia have been suggested to work conjunctively with the middle frontal gyrus to select information to be stored in working memory [78]. In addition, increased functional connectivity of the cingulo-opercular network (also referred to as the ventral attention/salience network) is associated with better performance on measures of fluid cognition (*e.g.*, executive function) in older adults [79]. The SVM identified critical current features in brain

regions previously associated with working memory performance and age-related cognitive decline, serving as an additional proof of principle for this approach.

4.3.   Future directions

The generated SVM model was highly accurate at classifying treatment responders in older adults, based only on the distributed patterns of electric current. Using these methods, precision tDCS dosing tailored to each individual can be generated to efficiently deliver equivalent current intensity within cortical regions that are essential for producing improvements in working memory. With optimization, application of these presented methods could potentially be expanded to improve tDCS efficiency in not only healthy older adults but also various mental health [7,80,81] and brain-based pathologies [8,9].

4.4.   Study limitations

The limited number of data points (n = 14) in the current study may affect the generalizability of the model. Thus in our future work, we will use a larger and more heterogeneous tDCS clinical trial dataset (n = 160) [82] (NCT02851511) which is near completion. To maximize the use of available data points and avoid overfitting in this study, we used two-level nested cross-validation to increase the number independent test samples and used 10 permutations to assess the retest reliability of these models. Average accuracy and confidence intervals across these permutations were used to estimate model performance on novel datasets. Our results show a 95% confidence interval of [85.03–87.83%] when the average accuracy is 86.42%, which demonstrates robust performance and small standard deviation of the classification performance. However, cross-validated analyses could lead to overoptimistic results. While efforts have been made to avoid overestimating the performance due to "double-dipping" in the choice of model hyperparameters [83] through nested cross-validation, results should be validated on an independent, larger cohort.

For simplicity of interpretation, we used a binary SVM to distinguish discrete classes: responders and non-responders. However, it is also feasible to utilize machine-learning algorithms to make continuous predictions (*i.e.*, magnitude of improvement). It should also be noted that misclassification of tissue continues to be a challenge for automated segmentation routines [84] which can influence subsequent FEM results since current density estimation is directly related to tissue organization and their assigned conductivity values. For instance, both bone and CSF compartments appear dark in T1-weighted images and thus bone tissue might be misclassified as CSF, or vice versa. This type of tissue misclassification can alter the amount of current entering the skull cavity [85] and thus affecting the estimated current found in the brain that was used for SVM classification. Therefore, the findings of the present study are limited by segmentation inaccuracy produced from the automated segmentation routines. Future studies are warranted to implement manual corrections to automated tissue segmentation and further analyze SVM results for automated versus manual segmentation process. Further, the present study serves as a proof of concept study for classification of tDCS responders and non-responders by utilizing features submitted to the classifier from the computational FEM. Introducing additional neuroimaging modalities and clinical data into the model may further enhance performance

and predictive value of machine-learning based approaches for understanding tDCS treatment response.

5. Conclusion

Clinical applications of tDCS have grown exponentially, yet reproducibility of these studies remains a challenge. At present, the optimal stimulation parameters remain unknown, making it difficult to ensure optimal treatment response on an individual basis. In this study, we proposed novel methods using FEM and SVM algorithms to detect the critical features of tDCS current, and identify stimulated cortical structures implicated in producing intended functional outcomes. We tested our methods in fourteen tDCS participants that underwent multiple days of stimulation at the F3–F4 locations. Our results demonstrated that current intensity has the strongest predictive value for treatment responders, with the performance of current direction only slightly inferior. These data suggest that reducing electrode displacement and delivering greater current intensity to essential brain regions implicated in treatment response are important for producing positive alterations in working memory performance. Future studies may include a larger cohort to generate more generalizable predictive models. Findings from this study can be coupled with customized electrode montages and dosing parameters to potentially enhance functional gains from tDCS treatment on an individual basis for a variety of therapeutic applications.

Supplementary Material

Refer to Web version on PubMed Central for supplementary material.

Acknowledgements

References

[1]. Knotkova H, Nitsche MA, Bikson M, Woods AJ, editors. Practical guide to transcranial direct current stimulation. Cham: Springer International Publishing; 2019 10.1007/978-3-319-95948-1.

[2]. Woods AJ, Antal A, Bikson M, Boggio PS, Brunoni AR, Celnik P, et al. A technical guide to tDCS, and related non-invasive brain stimulation tools. Clin Neurophysiol 2016;127:1031–48. 10.1016/j.clinph.2015.11.012. [PubMed: 26652115]

[3]. Bikson M, Grossman P, Thomas C, Zannou AL, Jiang J, Adnan T, et al. Safety of transcranial direct current stimulation: evidence based update 2016. Brain Stimul 2016 10.1016/j.brs.2016.06.004.

[4]. Nitsche MA, Cohen LG, Wassermann EM, Priori A, Lang N, Antal A, et al. Transcranial direct current stimulation: state of the art 2008. Brain Stimul 2008 10.1016/j.brs.2008.06.004.

[5]. Albizu A, Indahlastari A, Woods AJ. Non-invasive brain stimulation - encyclopedia of gerontology and population aging. In: Gu D, Dupre ME, editors. Cham: Springer International Publishing; 2019 p. 1–8. 10.1007/978-3-319-69892-2_682-1.

[6]. Rosen AC, Ramkumar M, Nguyen T, Hoeft F. Noninvasive transcranial brain stimulation and pain. Curr Pain Headache Rep 2009 10.1007/s11916-009-0004-2.

[7]. Clancy KJ, Baisley SK, Albizu A, Kartvelishvili N, Ding M, Li W. Lasting connectivity increase and anxiety reduction via transcranial alternating current stimulation. Soc Cognit Affect Neurosci 2018;13:1305–16. 10.1093/scan/nsy096. [PubMed: 30380131]

[8]. Chhatbar PY, Ramakrishnan V, Kautz S, George MS, Adams RJ, Feng W. Transcranial direct current stimulation post-stroke upper extremity motor recovery studies exhibit a dose-response relationship. Brain Stimul 2016 10.1016/j.brs.2015.09.002.

[9]. Datta A, Baker JM, Bikson M, Fridriksson J. Individualized model predicts brain current flow during transcranial direct-current stimulation treatment in responsive stroke patient. Brain Stimul 2011 10.1016/j.brs.2010.11.001.

[10]. Bikson M, Truong DQ, Mourdoukoutas AP, Aboseria M, Khadka N, Adair D, et al. Modeling sequence and quasi-uniform assumption in computational neurostimulation. Prog Brain Res 2015 10.1016/bs.pbr.2015.08.005.

[11]. Ranieri F, Podda MV, Riccardi E, Frisullo G, Dileone M, Profice P, et al. Modulation of LTP at rat hippocampal CA3-CA1 synapses by direct current stimulation. J Neurophysiol 2012 10.1152/jn.00319.2011.

[12]. Fritsch B, Reis J, Martinowich K, Schambra HM, Ji Y, Cohen LG, et al. Direct current stimulation promotes BDNF-dependent synaptic plasticity: potential implications for motor learning. Neuron 2010 10.1016/j.neuron.2010.03.035.

[13]. Artola A, Bröcher S, Singer W. Different voltage-dependent thresholds for inducing long-term depression and long-term potentiation in slices of rat visual cortex. Nature 1990 10.1038/347069a0.

[14]. Kronberg G, Bridi M, Abel T, Bikson M, Parra LC. Direct current stimulation modulates LTP and LTD: activity dependence and dendritic effects. Brain Stimul 2017 10.1016/j.brs.2016.10.001.

[15]. Kronberg G, Rahman A, Sharma M, Bikson M, Parra LC. Direct current stimulation boosts hebbian plasticity in vitro. Brain Stimul 2020 10.1016/j.brs.2019.10.014.

[16]. Márquez-Ruiz J, Leal-Campanario R, Sa chez-Campusano R, Molaee-Ardekani B, Wendling F, Miranda PC, et al. Transcranial direct-current stimulation modulates synaptic mechanisms involved in associative learning in behaving rabbits. Proc Natl Acad Sci U S A 2012 10.1073/pnas.1121147109.

[17]. Podda MV, Cocco S, Mastrodonato A, Fusco S, Leone L, Barbati SA, et al. Anodal transcranial direct current stimulation boosts synaptic plasticity and memory in mice via epigenetic regulation of Bdnf expression. Sci Rep 2016 10.1038/srep22180.

[18]. Nitsche MA, Paulus W. Excitability changes induced in the human motor cortex by weak transcranial direct current stimulation. J Physiol 2000 10.1111/j.1469-7793.2000.t01-1-00633.x.

[19]. Hoy KE, Arnold SL, Emonson MRL, Daskalakis ZJ, Fitzgerald PB. An investigation into the effects of tDCS dose on cognitive performance over time in patients with schizophrenia. Schizophr Res 2014 10.1016/j.schres.2014.03.006.

[20]. Esmaeilpour Z, Marangolo P, Hampstead BM, Bestmann S, Galletta E, Knotkova H, et al. Incomplete evidence that increasing current intensity of tDCS boosts outcomes. Brain Stimul 2018 10.1016/j.brs.2017.12.002.

[21]. Woods AJ, Bryant V, Sacchetti D, Gervits F, Hamilton R. Effects of electrode drift in transcranial direct current stimulation. Brain Stimul 2015 10.1016/j.brs.2014.12.007.

[22]. Opitz A, Yeagle E, Thielscher A, Schroeder C, Mehta AD, Milham MP. On the importance of precise electrode placement for targeted transcranial electric stimulation. Neuroimage 2018;181:560–7. 10.1016/j.neuroimage.2018.07.027. [PubMed: 30010008]

[23]. Radman T, Ramos RL, Brumberg JC, Bikson M. Role of cortical cell type and morphology in subthreshold and suprathreshold uniform electric field stimulation in vitro. Brain Stimul 2009 10.1016/j.brs.2009.03.007.

[24]. Jacobson L, Koslowsky M, Lavidor M. TDCS polarity effects in motor and cognitive domains: a meta-analytical review. Exp Brain Res 2012 10.1007/s00221-011-2891-9.

[25]. Rawji V, Ciocca M, Zacharia A, Soares D, Truong D, Bikson M, et al. tDCS changes in motor excitability are specific to orientation of current flow. Brain Stimul 2018 10.1016/j.brs.2017.11.001.

[26]. Indahlastari A, Albizu A, Nissim NR, Traeger KR, O'Shea A, Woods AJ. Methods to monitor accurate and consistent electrode placements in conventional transcranial electrical stimulation. Brain Stimul 2019;12:267–74. 10.1016/j.brs.2018.10.016. [PubMed: 30420198]

[27]. Thomas C, Datta A, Woods A. Effect of aging on cortical current flow due to transcranial direct current stimulation: considerations for safety. Proc. Annu. Int. Conf. IEEE Eng. Med. Biol. Soc EMBS 2018 10.1109/EMBC.2018.8513014.

[28]. Indahlastari A, Albizu A, O'Shea A, Forbes MA, Nissim NR, Kraft JN, et al. Modeling transcranial electrical stimulation in the aging brain. Brain Stimul 2020;13 10.1016/j.brs.2020.02.007.

[29]. Datta A, Bansal V, Diaz J, Patel J, Reato D, Bikson M. Gyri-precise head model of transcranial direct current stimulation: improved spatial focality using a ring electrode versus conventional rectangular pad. Brain Stimul 2009 10.1016/j.brs.2009.03.005.

[30]. Truong DQ, Magerowski G, Blackburn GL, Bikson M, Alonso-Alonso M. Computational modeling of transcranial direct current stimulation (tDCS) in obesity: impact of head fat and dose guidelines. NeuroImage Clin 2013 10.1016/j.nicl.2013.05.011.

[31]. Kessler SK, Minhas P, Woods AJ, Rosen A, Gorman C, Bikson M. Dosage considerations for transcranial direct current stimulation in children: a computational modeling study. PloS One 2013 10.1371/journal.pone.0076112.

[32]. Minhas P, Bikson M, Woods AJ, Rosen AR, Kessler SK. Transcranial direct current stimulation in pediatric brain: a computational modeling study. Proc. Annu. Int. Conf. IEEE Eng. Med. Biol. Soc EMBS 2012 10.1109/EMBC.2012.6346067.

[33]. Huang Y, Datta A, Bikson M, Parra LC. Realistic vOlumetric-Approach to Simulate Transcranial Electric Stimulation – ROAST – a fully automated open-source pipeline. J Neural Eng 2019 10.1088/1741-2552/ab208d.

[34]. Windhoff M, Opitz A, Thielscher A. Electric field calculations in brain stimulation based on finite elements: an optimized processing pipeline for the generation and usage of accurate individual head models. Hum Brain Mapp 2013 10.1002/hbm.21479.

[35]. Kasinadhuni AK, Indahlastari A, Chauhan M, Schär M, Mareci TH, Sadleir RJ. Imaging of current flow in the human head during transcranial electrical therapy. Brain Stimul 2017;10:764–72. 10.1016/j.brs.2017.04.125. [PubMed: 28457836]

[36]. Göksu C, Hanson LG, Siebner HR, Ehses P, Scheffler K, Thielscher A. Human in-vivo brain magnetic resonance current density imaging (MRCDI). Neuroimage 2018 10.1016/j.neuroimage.2017.12.075.

[37]. Huang Y, Liu AA, Lafon B, Friedman D, Dayan M, Wang X, et al. Measurements and models of electric fields in the in vivo human brain during transcranial electric stimulation. Elife 2017 10.7554/eLife.18834.

[38]. Indahlastari A, Kasinadhuni AK, Saar C, Castellano K, Mousa B, Chauhan M, et al. Methods to compare predicted and observed phosphene experience in TACS subjects. Neural Plast 2018 10.1155/2018/8525706.

[39]. Suen PJC, Doll S, Batistuzzo MC, Busatto G, Razza LB, Padberg F, et al. Association between tDCS computational modeling and clinical outcomes in depression: data from the ELECT-TDCS trial. Eur Arch Psychiatr Clin Neurosci 2020 10.1007/s00406-020-01127-w.

[40]. Antonenko D, Thielscher A, Saturnino GB, Aydin S, Ittermann B, Grittner U, et al. Towards precise brain stimulation: is electric field simulation related to neuromodulation? Brain Stimul 2019 10.1016/j.brs.2019.03.072.

[41]. Chang CC, Lin CJ. LIBSVM: a Library for support vector machines. ACM Trans Intell Syst Technol 2011 10.1145/1961189.1961199.

[42]. Mwangi B, Tian TS, Soares JC. A review of feature reduction techniques in Neuroimaging. Neuroinformatics 2014 10.1007/s12021-013-9204-3.

[43]. Dubois J, Galdi P, Han Y, Paul LK, Adolphs R. Resting-State functional brain connectivity best predicts the personality dimension of openness to experience. Personal Neurosci 2018 10.1017/pen.2018.8.

[44]. Kashyap R, Kong R, Bhattacharjee S, Li J, Zhou J, Thomas Yeo BT. Individual-specific fMRI-Subspaces improve functional connectivity prediction of behavior. Neuroimage 2019 10.1016/j.neuroimage.2019.01.069.

[45]. Mercer JXVI. Functions of positive and negative type, and their connection the theory of integral equations. Philos Trans R Soc Lond - Ser A Contain Pap a Math or Phys Character 1909 10.1098/rsta.1909.0016.

[46]. Guyon I, Boser B, Vapnik V. Automatic capacity tuning of very large VC-dimension classifiers. Adv Neural Inf Process Syst 1993.

[47]. Li J, Kong R, Liégeois R, Orban C, Tan Y, Sun N, et al. Global signal regression strengthens association between resting-state functional connectivity and behavior. Neuroimage 2019 10.1016/j.neuroimage.2019.04.016.

[48]. Kambeitz J, Goerigk S, Gattaz W, Falkai P, Benseñor IM, Lotufo PA, et al. Clinical patterns differentially predict response to transcranial direct current stimulation (tDCS) and escitalopram in major depression: a machine learning analysis of the ELECT-TDCS study. J Affect Disord 2020 10.1016/j.jad.2020.01.118.

[49]. Nissim NR, O'Shea A, Indahlastari A, Kraft JN, von Mering O, Aksu S, et al. Effects of transcranial direct current stimulation paired with cognitive training on functional connectivity of the working memory network in older adults. Front Aging Neurosci 2019 10.3389/fnagi.2019.00340.

[50]. Li X, Morgan PS, Ashburner J, Smith J, Rorden C. The first step for neuroimaging data analysis: DICOM to NIfTI conversion. J Neurosci Methods 2016 10.1016/j.jneumeth.2016.03.001.

[51]. Morey RA, Petty CM, Xu Y, Pannu Hayes J, Wagner HR, Lewis DV, et al. A comparison of automated segmentation and manual tracing for quantifying hippocampal and amygdala volumes. Neuroimage 2009 10.1016/j.neuroimage.2008.12.033.

[52]. Cardinale F, Chinnici G, Bramerio M, Mai R, Sartori I, Cossu M, et al. Validation of FreeSurfer-estimated brain cortical thickness: comparison with histologic measurements. Neuroinformatics 2014 10.1007/s12021-014-9229-2.

[53]. Qianqian Fang, Boas DA. Tetrahedral mesh generation from volumetric binary and grayscale images. IEEE Int. Symp. Biomed. Imaging From Nano to Macro, IEEE; 2009, 10.1109/ISBI.2009.5193259; 2009 1142–1145.

[54]. Dular P, Geuzaine C, Henrotte F, Legros W. A general environment for the treatment of discrete problems and its application to the finite element method. IEEE Trans Magn 1998 10.1109/20.717798.

[55]. Huang Y, Dmochowski JP, Su Y, Datta A, Rorden C, Parra LC. Automated MRI segmentation for individualized modeling of current flow in the human head. J Neural Eng 2013 10.1088/1741-2560/10/6/066004.

[56]. Ashburner J A fast diffeomorphic image registration algorithm. Neuroimage 2007 10.1016/j.neuroimage.2007.07.007.

[57]. Saeys Y, Inza I, Larrañaga P. A review of feature selection techniques in bio-informatics. Bioinformatics 2007 10.1093/bioinformatics/btm344.

[58]. Guyon I, Elisseeff A. An introduction to variable and feature selection. J Mach Learn Res 2003 10.1162/153244303322753616.

[59]. Steinwart I, Christmann A. Support vector machines. Springer Science & Business Media; 2008.

[60]. Varoquaux G, Raamana PR, Engemann DA, Hoyos-Idrobo A, Schwartz Y, Thirion B. Assessing and tuning brain decoders: cross-validation, caveats, and guidelines. Neuroimage 2017 10.1016/j.neuroimage.2016.10.038.

[61]. Polosecki P, Castro E, Rish I, Pustina D, Warner JH, Wood A, et al. Resting-state connectivity stratifies premanifest Huntington's disease by longitudinal cognitive decline rate. Sci Rep 2020 10.1038/s41598-020-58074-8.

[62]. Lindquist MA, Krishnan A, López-Solà M, Jepma M, Woo CW, Koban L, et al. Group-regularized individual prediction: theory and application to pain. Neuroimage 2017 10.1016/j.neuroimage.2015.10.074.

[63]. Cole JH, Leech R, Sharp DJ. Prediction of brain age suggests accelerated atrophy after traumatic brain injury. Ann Neurol 2015 10.1002/ana.24367.

[64]. Goldstein JM, Seidman LJ, Makris N, Ahern T, O'Brien LM, Caviness VS, et al. Hypothalamic abnormalities in schizophrenia: sex effects and genetic vulnerability. Biol Psychiatr 2007 10.1016/j.biopsych.2006.06.027.

[65]. Statistics Mathworks. Machine learning toolbox ™ user's guide R2019b. 2019 MatLab.

[66]. Hedges LV. Distribution theory for glass's estimator of effect size and related estimators. J Educ Stat 1981 10.2307/1164588.

[67]. Smirnov N Table for estimating the goodness of fit of empirical distributions. Ann Math Stat 1948 10.1214/aoms/1177730256.

[68]. Massey FJ. The Kolmogorov-smirnov test for goodness of fit. J Am Stat Assoc 1951 10.1080/01621459.1951.10500769.

[69]. Fawcett T ROC graphs: notes and practical considerations for researchers. Mach Learn 2004.

[70]. Mosayebi Samani M, Agboada D, Jamil A, Kuo MF, Nitsche MA. Titrating the neuroplastic effects of cathodal transcranial direct current stimulation (tDCS) over the primary motor cortex. Cortex 2019 10.1016/j.cortex.2019.04.016.

[71]. Ramaraju S, Roula MA, McCarthy PW. Modelling the effect of electrode displacement on transcranial direct current stimulation (tDCS). J Neural Eng 2018 10.1088/1741-2552/aa8d8a.

[72]. Thomas Yeo BT, Krienen FM, Sepulcre J, Sabuncu MR, Lashkari D, Hollinshead M, et al. The organization of the human cerebral cortex estimated by intrinsic functional connectivity. J Neurophysiol 2011 10.1152/jn.00338.2011.

[73]. D'Esposito M, Postle BR, Ballard D, Lease J. Maintenance versus manipulation of information held in working memory: an event-related fMRI study. Brain Cognit 1999 10.1006/brcg.1999.1096.

[74]. Petrides M Dissociable roles of mid-dorsolateral prefrontal and anterior inferotemporal cortex visual working memory. J Neurosci 2000 10.1523/JNEUROSCI.20-19-07496.2000.

[75]. Blumenfeld RS, Nomura EM, Gratton C, D'Esposito M. Lateral prefrontal cortex is organized into parallel dorsal and ventral streams along the rostro-caudal axis. Cerebr Cortex 2013 10.1093/cercor/bhs223.

[76]. Nissim NR, O'Shea A, Indahlastari A, Telles R, Richards L, Porges E, et al. Effects of in-scanner bilateral frontal tDCS on functional connectivity of the working memory network in older adults. Front Aging Neurosci 2019 10.3389/fnagi.2019.00051.

[77]. Packard MG, Knowlton BJ. Learning and memory functions of the basal ganglia. Annu Rev Neurosci 2002 10.1146/annurev.neuro.25.112701.142937.

[78]. McNab F, Klingberg T. Prefrontal cortex and basal ganglia control access to working memory. Nat Neurosci 2008 10.1038/nn2024.

[79]. Hausman HK, O'Shea A, Kraft JN, Boutzoukas EM, Evangelista ND, Van Etten EJ, et al. The role of resting-state network functional connectivity in cognitive aging. Front Aging Neurosci 2020 10.3389/fnagi.2020.00177.

[80]. Clancy KJ, Albizu A, Schmidt NB, Li W. Intrinsic sensory disinhibition contributes to intrusive re-experiencing in combat veterans. Sci Rep 2020;10:936 10.1038/s41598-020-57963-2. [PubMed: 31969671]

[81]. Szymkowicz SM, McLaren ME, Suryadevara U, Woods AJ. Transcranial direct current stimulation use in the treatment of neuropsychiatric disorders: a brief review. Psychiatr Ann 2016 10.3928/00485713-20161006-01.

[82]. Woods AJ, Cohen R, Marsiske M, Alexander GE, Czaja SJ, Wu S. Augmenting cognitive training in older adults (The ACT Study): design and Methods of a Phase III tDCS and cognitive training trial. Contemp Clin Trials 2018;65:19–32. 10.1016/j.cct.2017.11.017. [PubMed: 29313802]

[83]. Varma S, Simon R. Bias in error estimation when using cross-validation for model selection. BMC Bioinf 2006 10.1186/1471-2105-7-91.

[84]. Kazemi K, Noorizadeh N. Quantitative comparison of SPM, FSL, and brainsuite for brain MR image segmentation. J Biomed Phys Eng 2014.

[85]. Laakso I, Tanaka S, Koyama S, De Santis V, Hirata A. Inter-subject variability in electric fields of motor cortical tDCS. Brain Stimul 2015 10.1016/j.brs.2015.05.002.
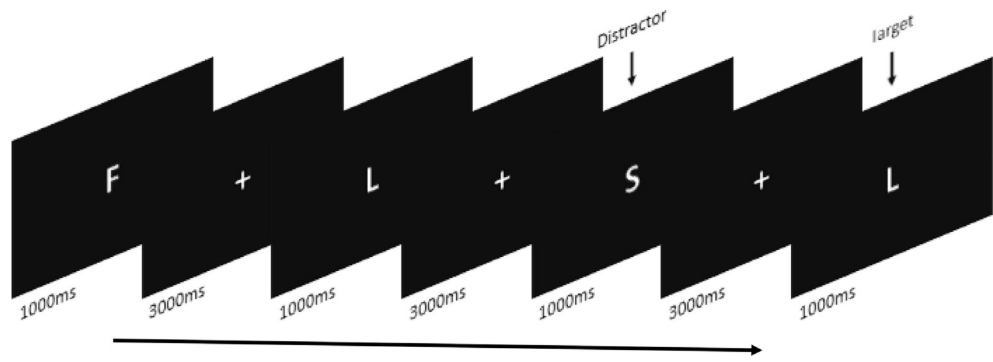
Fig. 1.
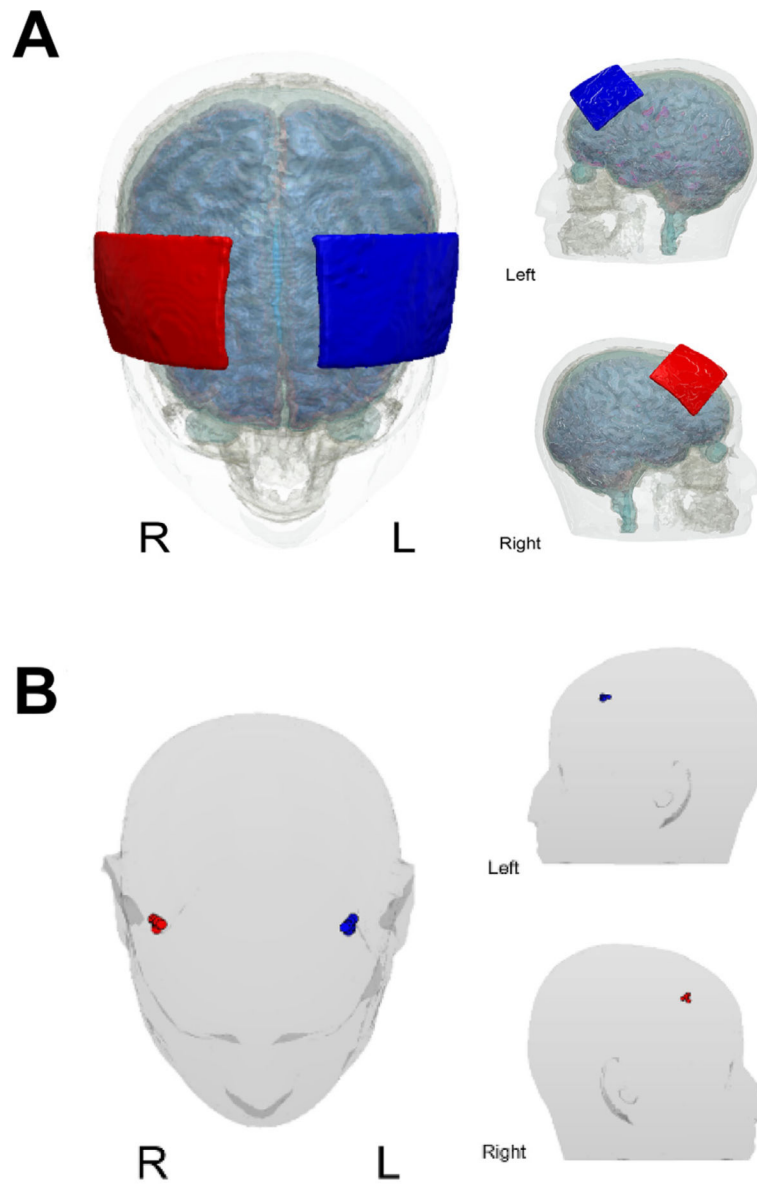An example of the stimulus presentation in the two-back variant of the N-back task.

Fig. 2.
A) The F3-F4 electrode montage with the F3 electrode as the cathode (blue) and the F4 electrode as the anode (red). B) A representative image of actual anode (red) and cathode (blue) placements for a single subject across ten sessions. The mean displacement for this participant of the anode and cathode was 1.9 cm (−0.2 St. Dev.) and 1.7 cm (−0.45 St. Dev.), respectively.

A

B
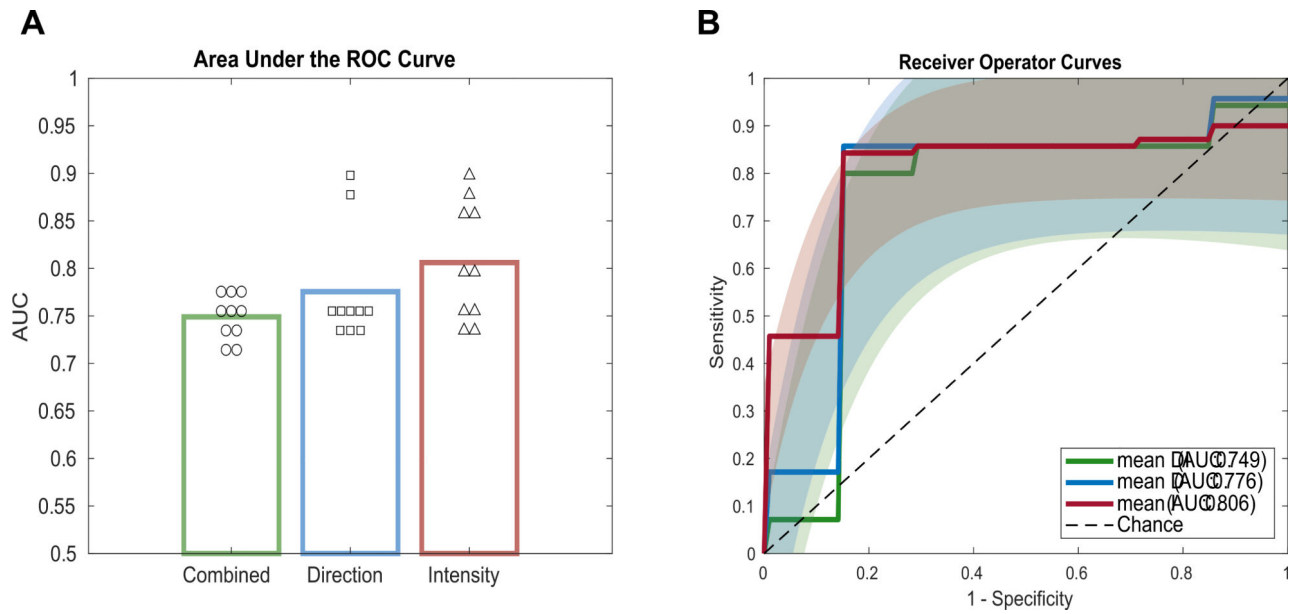
Fig. 3.
A) Areas under the ROC curve across ten iterations of three data types: direction, intensity, and combined. Mean AUC plotted as bars. No significant difference was observed. B) The mean ROC curve of each model across ten iterations with shaded area conveying 95% confidence interval.
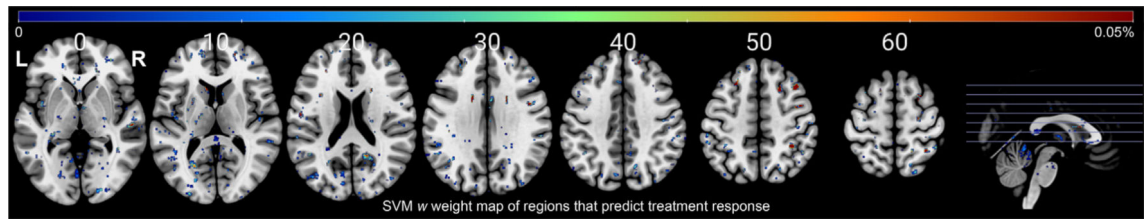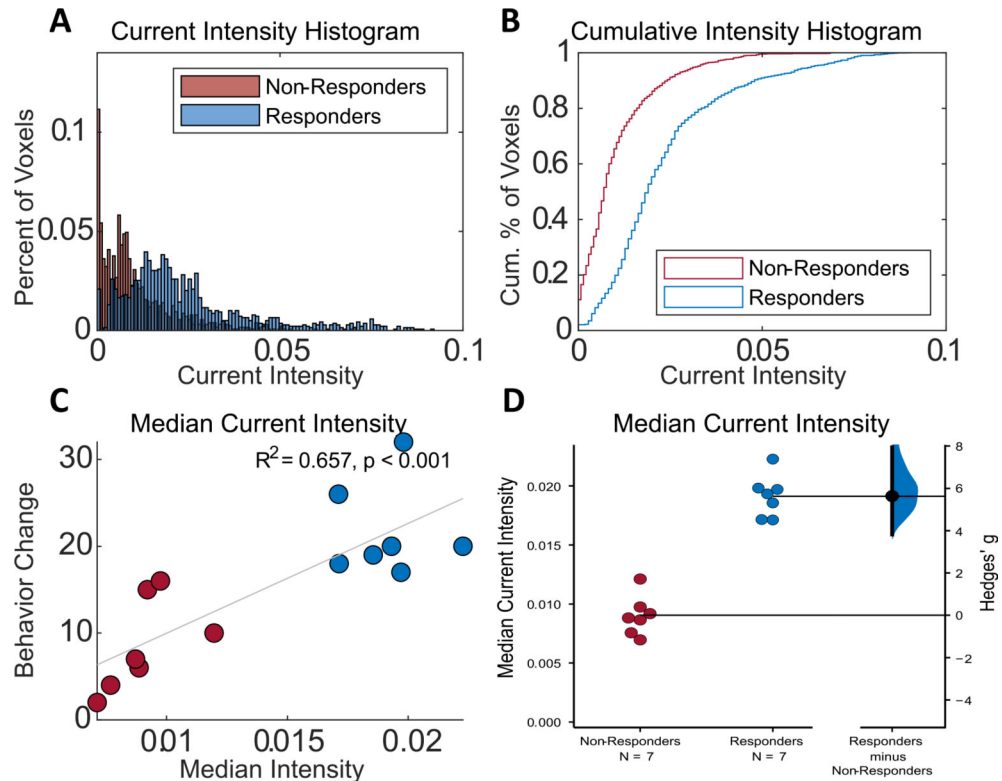
Fig. 4.
Discrimination maps of regions that predict working memory improvements with the percent contribution of each voxel to the SVM decision function, superimposed onto the MNI152 Template.

Fig. 5.
Plots to demonstrate the current density characteristics within regions predictive of tDCS responders. A) Histogram of current intensity (bin width of 0.0013 Am-2) with the y-axis representing the number of observations in each bin divided by the total number of observations, where the sum of all bar heights is equal to 1. B) Cumulative histogram of current intensity with the height of each step equal to the cumulative number of observations in the bin over the total number of observations in each bin and all previous bins where the height of the last bar is equal to 1. C) Scatter plot of behavior change (post – pre intervention working memory performance) vs. median current intensity. D) The Hedges' g between responders and non-responders is shown in a Gardner-Altman estimation plot. The mean difference is plotted on a floating axis as a bootstrap sampling distribution. The mean difference is depicted as a dot; the 95% confidence interval is indicated by the ends of the vertical error bar.
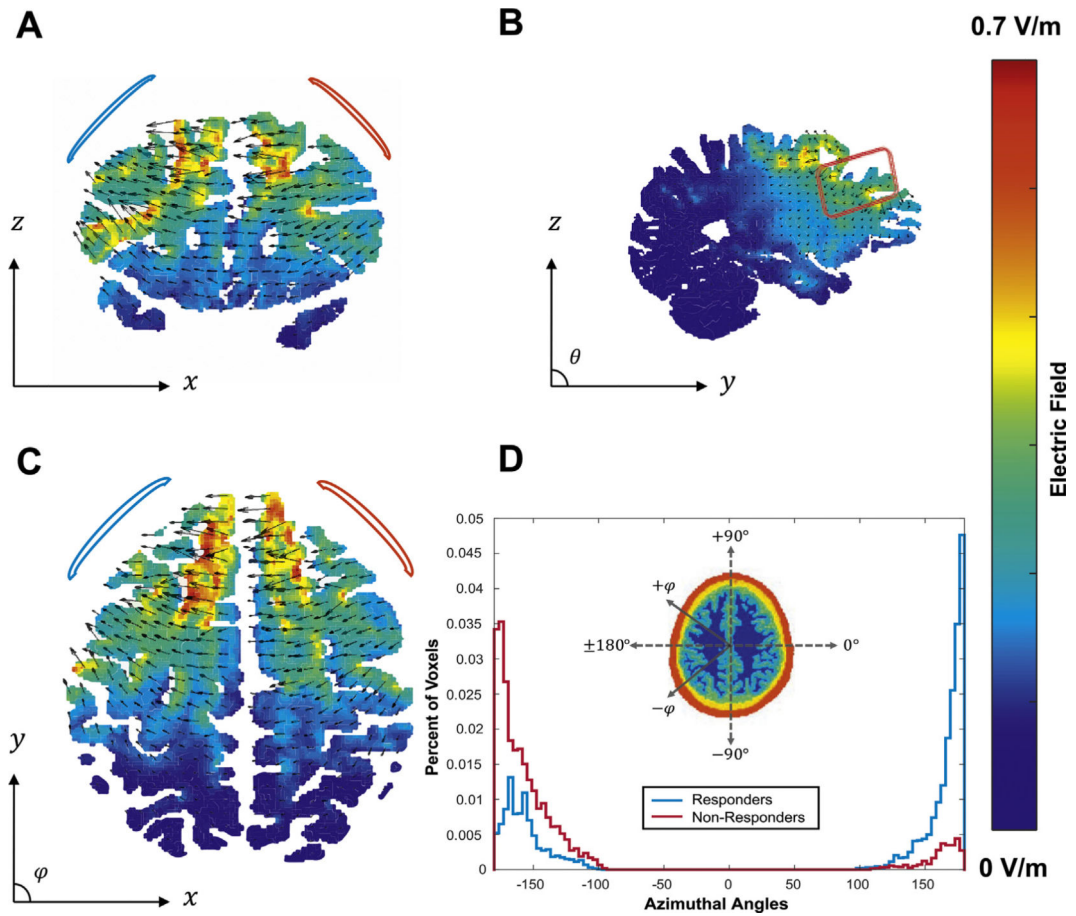
Fig. 6.
Single representative participant A) Coronal, B) Sagittal, and C) Axial image of current intensity represented by the color of the images, and current direction represented by the arrows within the images. The color bar represents electric field in volts per meter (*v/m*). D) Histogram of azimuthal angle δ with the height of each bar representing the number of observations in each bin divided by the total number of observations, where the sum of the all bar heights is equal to 1.
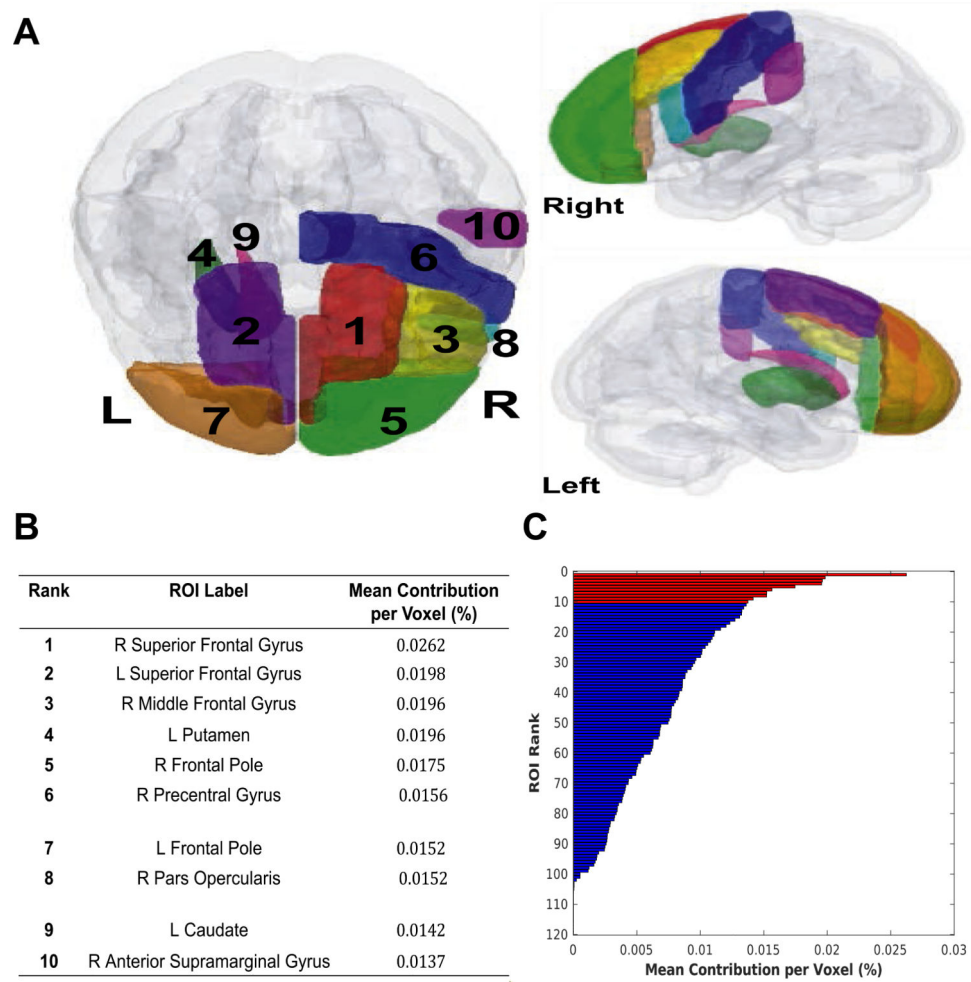
Fig. 7.
A) Visualization of the top 10 regions of interest from the Harvard-Oxford atlas ranked based on their contribution toward predictions of treatment response. B) Rank, label, and mean percent contribution per voxel of the top ten regions of interest. C) a bar graph to represent the average percent contribution per voxel within each ROI of Harvard-Oxford atlas with the top 10 regions of interest highlighted in red.
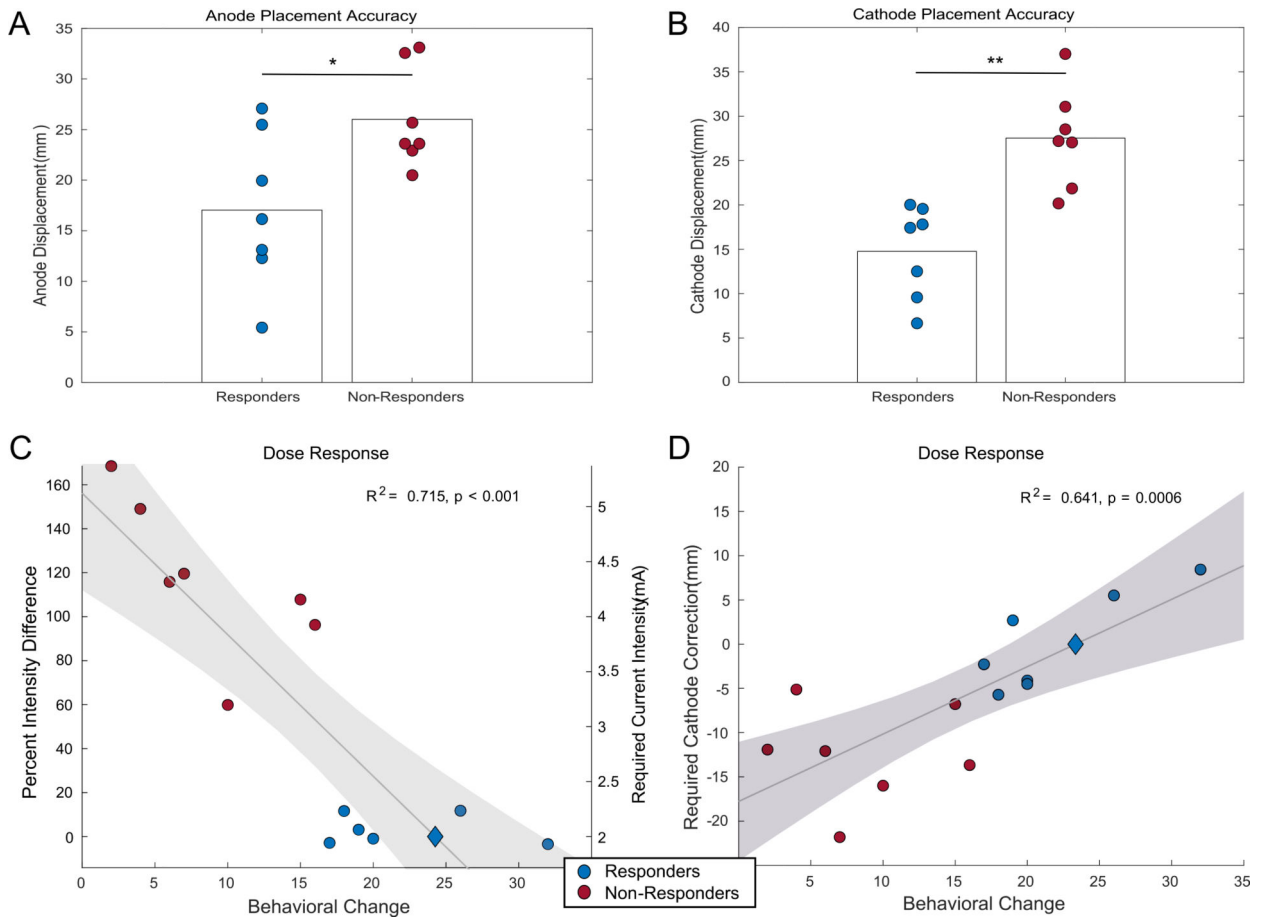
Fig. 8.
A) Anode and B) Cathode displacement between responders and non-responders, with means plotted as bars. Non-responders were found to have greater displacement of both electrodes (anode: $F2 = 6.73$, $P = 0.023$, cathode: $F2 = 19.39$, $p < 0.001$) from their ideal placement compared to responders. Linear regression of C) current intensity and D) current direction, based on the percent difference of average current intensity and cathode displacement versus behavioral change. The optimal stimulation parameters are represented by the diamond in the figure (i.e., the mean within the responder group). * represents $p < 0.05$ and ** represents $p < 0.01$).

Table 1.

A summary table of SVM model performance metrics using ROAST tissue conductivity values [33]: Average Test Accuracy (ACC) with [95% Confidence Interval], Area under the ROC curve (AUC), F1 Score (F1), and Matthews Correlation Coefficient (MCC) for intensity, direction, and direction x intensity of current density.

Intensity				Direction				Direction x Intensity			
ACC	AUC	F1	MCC	ACC	AUC	F1	MCC	ACC	AUC	F1	MCC
86.46 [85.03 – 87.83]	0.806	0.86	0.73	86.46 [85.03 – 87.83]	0.776	0.86	0.73	86.46 [85.03 – 87.83]	0.749	0.86	0.73